

1 **Different effects of anthropogenic emissions and aging processes on the**
2 **mixing state of soot particles in the nucleation and accumulation**
3 **modes**

4
5 Yuying Wang^{1,2}, Rong Hu^{1,2}, Qiuyan Wang¹, Zhanqing Li³, Maureen Cribb³, Yele Sun⁴, Xiaorui
6 Song¹, Yi Shang¹, Yixuan Wu¹, Xin Huang¹, Yuxiang Wang¹

7
8 ¹Key Laboratory for Aerosol-Cloud-Precipitation of China Meteorological Administration, School
9 of Atmospheric Physics, Nanjing University of Information Science & Technology, Nanjing
10 210044, China

11 ²State Key Laboratory of Remote Sensing Science, College of Global Change and Earth System
12 Science, Beijing Normal University, Beijing 100875, China

13 ³Earth System Science Interdisciplinary Center, Department of Atmospheric and Oceanic Science,
14 University of Maryland, College Park, MD, USA

15 ⁴State Key Laboratory of Atmospheric Boundary Layer Physics and Atmospheric Chemistry,
16 Institute of Atmospheric Physics, Chinese Academy of Sciences, Beijing, 100029, China

17
18 Correspondence to: Yuying Wang (yuyingwang@nuist.edu.cn)

19 **Abstract.** In this study, the mixing state of size-resolved soot particles and their influencing factors
20 were investigated based on a five-month aerosol volatility measurement at a suburban site (Xingtai,
21 XT) in the central North China Plain (NCP). The volatility and mixing state of soot-containing
22 particles at XT were complex caused by multiple pollution sources and various aging processes.
23 The results suggest that anthropogenic emissions can weaken the mean volatility of soot-containing
24 particles and enhance their degree of external mixing. There were fewer externally mixed soot
25 particles in warm months (June, July, and August) than in cold months (May, September, and
26 October). Monthly variations in the mean coating depth ($D_{c,mean}$) of volatile matter on soot particles
27 showed that the coating effect was stronger in warm months than in cold months, even though
28 aerosol pollution was heavier in cold months. Moreover, the volatility was stronger, and the degree
29 of internal mixing was higher in nucleation-mode soot-containing particles than in accumulation-
30 mode soot-containing particles. Relationships between $D_{c,mean}$ and possible influencing factors
31 [temperature (T), relative humidity (RH), and particulate matter with diameters ranging from 10 to
32 400 nm] further suggest that high ambient T and RH in a polluted environment could promote the
33 coating growth of accumulation-mode soot particles. However, high ambient T but low RH in a
34 clean environment were beneficial to the coating growth of nucleation-mode soot particles. Our
35 results highlight the diverse impact of anthropogenic emissions and aging processes on the mixing
36 state of soot particles in different modes, which should be considered separately in models to
37 improve the simulation accuracy of aerosol absorption.

38

39 1. Introduction

40 Aerosols are mixed liquid and solid particles suspended in the atmosphere. Some aerosols are
41 directly produced from natural or anthropogenic sources (i.e., primary aerosols), and the rest are
42 indirectly transformed from gas precursors through atmospheric chemical reactions (i.e., secondary
43 aerosols). The newly formed particles can grow or shrink through various aging processes (e.g.,
44 condensation, coagulation, volatilization, chemical reactions). Aerosol physicochemical properties
45 (number concentration, shape, mixing state, optical properties, among others) are thus highly
46 variable. This is one of the reasons why aerosols are highly uncertain in climate change assessments
47 (Bond et al., 2013; Seinfeld et al., 2016; Bellouin et al., 2020; Christensen et al., 2021). Although
48 great efforts have been made to understand aerosol optical properties, the uncertainty of radiative
49 forcing caused by aerosols is still two to three times that of greenhouse gases (IPCC, 2021).

50 Aerosols can affect the earth-atmosphere radiation balance by scattering or absorbing shortwave
51 and longwave radiation, which is called the aerosol direct climate effect or aerosol-radiation
52 interactions. Many factors, such as aerosol chemical composition, mixing state, and ambient relative
53 humidity (RH), have complex impacts on aerosol-radiation interactions (e.g., Twohy et al., 2009;

54 Kuniyal and Guleria, 2019; Ren et al., 2021). According to the sixth IPCC report, the total direct
55 radiative forcing caused by anthropogenic aerosols is generally negative. However, light-absorbing
56 carbonaceous particles (LAC) have a warming effect on climate (Ramana et al., 2010; Gustafsson
57 and Ramanathan, 2016), which can partly offset the cooling effect caused by scattering aerosols,
58 such as sulfate. Black carbon (BC) is the most important LAC compound, mostly emitted as soot
59 from anthropogenic sources (incomplete fossil fuel combustion and biomass burning) (Novakov et
60 al., 2003). Some experiments have suggested that BC in urban polluted environments can play an
61 important role in pollution formation and development. The internal mixing of BC with secondly
62 formed matter could also greatly enhance light absorption (Peng et al., 2016; Zhou et al., 2017).
63 ~~However, studies on the mixing state of BC or soot particles in the actual atmosphere are few due~~
64 ~~to limited observations.~~

65 The online measurement instruments quantifying the mixing state of BC-containing particles are
66 limited. Based on the measurement of single-particle soot photometer (SP2), Wu et al. (2017)
67 indicated that the mass of refractory black carbon (r_{BC}) had an approximately lognormal
68 distribution as a function of the volume-equivalent diameter (VED) in Beijing. Yu et al. (2020)
69 suggested that the mixing state of r_{BC} particles was related to air pollution levels and air mass
70 sources. Zhang et al. (2021) further indicated that meteorological conditions had a large impact on
71 the mixing state of r_{BC} particles. Moreover, the Aerodyne soot particle aerosol mass spectrometer
72 (SP-AMS) can also be used to study the mixing state of r_{BC} . For example, J. Wang et al. (2019)
73 found that the formation of secondary aerosols through photochemical and aqueous chemical
74 reactions was responsible to the coating of r_{BC} based on the measurement of SP-AMS in winter
75 Beijing. However, the lower observation limit of particle size by SP2 and SP-AMS is larger than
76 ~70 nm. Therefore, they cannot quantify the mixing state of BC-containing particles in the small
77 nucleation mode.

78
79 Aerosol volatility refers to the shrinking extent of particles at a certain temperature. The mixing
80 state of soot particles or tarballs is closely related to aerosol volatility at high temperatures (Philippin
81 et al., 2004; Wehner et al., 2009; Adachi et al., 2018, 2019). ~~This is because m~~Most primary soot
82 particles from anthropogenic sources are refractory, hydrophobic, and externally mixed. In a
83 polluted environment, primary soot particles are easily transformed to internally mixed particles
84 through certain coating processes in the atmosphere (Cheng et al., 2012; Peng et al., 2016; F. Zhang
85 et al., 2020). However, coating matter is generally non-refractory because most of the matter
86 consists of secondary chemical species, such as organics, sulfate, and nitrate (Philippin et al., 2004;
87 Hong et al., 2017). This is why aerosol volatility can characterize the mixing state of soot particles
88 in pollute environments (Wehner et al., 2009; Hossain et al., 2012; S. Zhang et al., 2016). A volatility

带格式的: 字体: (默认) Times New Roman, 五号, 字体颜色: 自动设置, 图案: 清除

带格式的: 字体: (默认) Times New Roman, 五号, 倾斜, 字体颜色: 自动设置, 图案: 清除

带格式的: 字体: (默认) Times New Roman, 五号, 字体颜色: 自动设置, 图案: 清除

带格式的: 字体颜色: 文字 1

带格式的: 字体: 倾斜, 字体颜色: 文字 1

带格式的: 字体颜色: 文字 1

带格式的: 字体: 倾斜, 字体颜色: 文字 1

带格式的: 字体颜色: 文字 1

带格式的: 字体颜色: 文字 1

带格式的: 字体: 倾斜

带格式的: 字体: (默认) Times New Roman, 五号

带格式的: 字体: 倾斜

带格式的: 缩进: 首行缩进: 1 字符

带格式的: 字体颜色: 自动设置

带格式的: 字体: (默认) Times New Roman, (中文) + 中文正文 (等线), 五号, 字体颜色: 自动设置, 英语(美国)

带格式的: 字体: (默认) Times New Roman, (中文) + 中文正文 (等线), 五号, 字体颜色: 自动设置, 英语(美国)

带格式的: 字体颜色: 自动设置

89 tandem differential mobility analyzer (VTDMA) is usually used to quantify aerosol volatility by
90 measuring the change in particle size at a set temperature. Aerosol volatility measured by a VTDMA
91 at a high temperature (> 280°C) can be used to study the mixing state of soot particles (Philippin et
92 al., 2004; Wehner et al., 2009; Y. Zhang et al., 2016; Wang et al., 2017). Meanwhile, VTDMA
93 measurements are based on the aerosol number concentration, which is always high in the nucleation
94 mode in the actual atmosphere. Therefore, VTDMA can quantify the mixing state of nucleation-
95 mode soot particles.

带格式的: 字体颜色: 自定义颜色(RGB(8,0,0))

带格式的: 字体颜色: 自定义颜色(RGB(8,0,0))

带格式的: 字体颜色: 自定义颜色(RGB(8,0,0))

带格式的: 字体颜色: 自定义颜色(RGB(8,0,0))

带格式的: 字体颜色: 自定义颜色(RGB(8,0,0))

96 Over the past years, several studies have reported the volatility and mixing state of soot-
97 containing particles based on VTDMA measurements in the North China Plain (NCP). For example,
98 Wehner et al. (2009) found that the mixing state of soot particles in Beijing and its surrounding
99 region varied, especially between new particle formation days and heavily polluted days. Using the
100 same VTDMA and aerosol optical data, Cheng et al. (2009) conducted an aerosol optical closure
101 study, finding that soot aging was rapid at the Yufa site south of Beijing. The coating on soot particles
102 can enhance aerosol absorption and scattering coefficients by a factor of 8 to 10 within several hours
103 due to secondary processing during the daytime, which is the combined effect of the increased
104 thickness of the coating shell and the transition of soot from an externally mixed state to a coated
105 state. Cheng et al. (2012) further indicated that aging and emissions were two competing factors in
106 the mixing state of soot particles. Based on VTDMA measurement data collected in 2015, Wang et
107 al. (2017) indicated that strict emission control measures implemented in Beijing and surrounding
108 areas could enhance the volatility of soot-containing particles and their degrees of external mixing.
109 At another regional site (Xi^anghe) in the northern part of the NCP, S. Zhang et al. (2016) found that
110 the mixing state of ambient particles was complex with different volatilities. Furthermore, Y. Zhang
111 et al. (2016) suggested that the average shell-to-core ratio and absorption enhancement (E_{ab}) of
112 ambient BC was 2.1–2.7 and 1.6–1.9, respectively.

113 These studies imply that anthropogenic emissions play an important role in the volatility and
114 mixing state of soot-containing particles and that the coating on soot particles can greatly enhance
115 aerosol absorption. However, these studies were based on data collected during short-term
116 observational periods in the northern part of the NCP and they did not distinguish the factors
117 influencing the mixing state of nucleation- and accumulation-mode soot particles. Recent studies
118 (Y. Wang et al., 2018, 2019, 2021) have shown that anthropogenic sources and aerosol aging
119 processes are various in the north and central-south NCP, leading to diverse aerosol physiochemical
120 properties between these regions in different seasons. More research about the volatility and mixing
121 state of soot particles in the central-south NCP is needed to improve the accuracy of modeled aerosol
122 optical properties.

123 This study investigates for the first time the volatility and mixing state of nucleation- and

124 accumulation-mode soot-containing particles in the warm and cold seasons based on one
125 comprehensive field campaign that took place in the central NCP, lasting five months. Exploring
126 factors influencing the volatility and mixing state of soot-containing particles in this study will
127 improve the accuracy of modeled aerosol optical properties in the central NCP. This paper is
128 organized as follows. Section 2 introduces the sampling site, instruments, and data analysis. Section
129 3 presents the results and discussion, including meteorological conditions, aerosol pollution levels,
130 changes in volatility and mixing state of soot-containing particles, and their influencing factors.
131 Section 4 gives conclusions and summarizes the study.
132

133 2. Sampling site, instruments, and data analysis

134 2.1 Sampling site

135 Data used in this study were collected at the National Meteorological Basic Station (37°11'N,
136 114°22'E, 180 m above sea level) in Xingtai (XT), China, equipped with a variety of meteorological
137 observation instruments. The measured meteorological variables including ambient temperature,
138 relative humidity (RH), wind direction and speed was used in this study. Y. Wang et al. (2018)
139 reported that this site is located in a polluted area of the central-south NCP, influenced by multiple
140 anthropogenic sources, such as industrial coal firing, fossil-fuel burning, agricultural activities, and
141 household emissions. The long-distance transport of pollutants also influences the air quality at XT.
142 Previous studies have suggested that air pollution at XT represents well regional pollution
143 characteristics in the central NCP east of the Taihang Mountains (Y. Zhang et al., 2018; Y. Wang et
144 al., 2018). A comprehensive field campaign named the Atmosphere-Aerosol-Boundary layer-Cloud
145 (A²BC) Interaction Joint Experiment was carried out at XT from May to October of 2016. Y. Wang
146 et al. (2018) and Li et al. (2019) provide details about the XT site and the A²BC campaign. Here,
147 over five months of aerosol observational data, including particle number size distribution (PNSD),
148 aerosol volatility, and BC mass concentration, were used to analyze the volatility and mixing state
149 of soot particles and their influencing factors.

150

151 2.2 Instruments

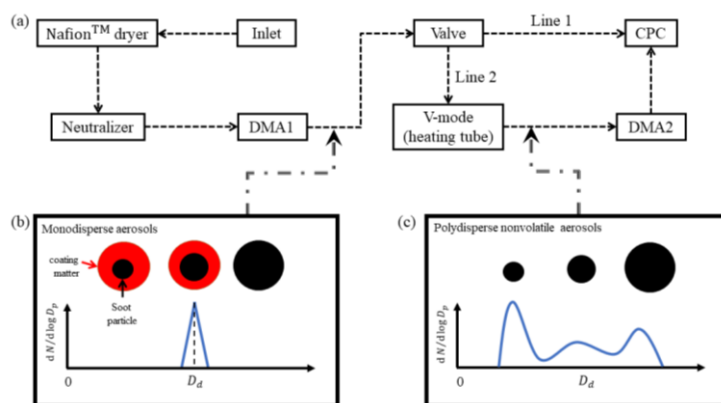
152 2.2.1 Measuring PNSD and aerosol volatility

153 The tandem differential mobility analyzer (TDMA) system is widely used to measure the change
154 in particle size under special conditions, e.g., high humidity, high temperature, and chamber
155 chemical reactions (Swietlicki et al., 2008). In this campaign, the VTDMA system was used to
156 measure aerosol volatility at 300°C. The inlet air sample was first dried by a Nafion™ dryer to low
157 RH (< 30%), then neutralized by a soft X-ray neutralizer (model 3088, TSI Inc.; Fig. 1a). Afterwards,
158 quasi-monodisperse aerosols (Fig. 1b) with a certain dried diameter (D_d) were split by the first

159 differential mobility analyzer (DMA1). In this campaign, D_d was set to 40, 80, 110, 150, 200, and
 160 300 nm. An automated valve located after the DMA1 had two outlet lines. Line 1 directly accessed
 161 the water-based condensation particle counter (WCPC, model 3787, TSI Inc.), measuring the ~~PNSD~~
 162 number concentration of particles ~~sizes~~ ranging from 10 to 400 nm. Line 2 accessed a heating tube,
 163 vaporizing volatile materials at a controlled high temperature (300°C in this study). The ratio of
 164 particle size after volatilization [$D_p(T)$] to D_d is defined as the aerosol shrink factor (i.e., $SF = D_p(T)$
 165 / D_d). After heating, residual aerosols were generally polydisperse nonvolatile particles (Fig. 1c).
 166 The second DMA (DMA2) and WCPC were used to measure the number size distribution of
 167 nonvolatile particles, measuring the distribution function of SF (SF -MDF). Finally, the probability
 168 density function of SF (SF -PDF) was retrieved using the TDMAfit algorithm (Stolzenburg and
 169 McMurry, 1988; Stolzenburg and McMurry, 2008).

170 In this study, we assume that the shape of all particles follows the core-shell model (nonvolatile
 171 core and volatile shell; Fig. 1b). Residual particles after volatilization have different-sized
 172 nonvolatile cores (Fig. 1c). Previous studies have suggested that residual particles at 300°C mainly
 173 consist of soot (Philippin et al., 2004; Wehner et al., 2009). Aerosol volatility measured by the
 174 VTDMA in this study can thus reflect the degree of mixing state of soot particles.

175



176

177 **Figure 1.** Schematic diagram of the volatility tandem differential mobility analyzer used in this
 178 study.

179

180 2.2.2 Measuring BC

181 ~~BC aerosols are mainly emitted from incomplete combustion of carbon-containing fuels,~~
 182 ~~including vehicle exhaust, coal, and biomasses (Novakov et al., 2003).~~ In this campaign, a seven-
 183 wavelength aethalometer (model AE-33, Magee Scientific Corp.) was used to measure the mass
 184 concentration of BC (M_{BC}). After calibration, the sampling flow rate of the AE-33 was 5.0 L min⁻¹.

185 A cyclone with particulate matter (diameters = 2.5 μm , or $\text{PM}_{2.5}$) was used in the sample inlet.
 186 Aerosol particles were collected on filter tape through a spot, and the instantaneous concentration
 187 of optically absorbing aerosols was retrieved from the rate of change of the attenuation of light
 188 transmitted through the filter. The wavelength channels of the AE-33 were 370, 470, 525, 590, 660,
 189 880, and 940 nm. According to the manufacturer's instructions, the M_{BC} is calculated from the
 190 change in optical attenuation at channel 6 (i.e., 880 nm) in the selected time interval using the mass
 191 absorption cross section (MAC) of 7.77 $\text{m}^2 \text{g}^{-1}$. The dependency of MAC on BC coating may
 192 introduce some uncertain in calculating MAC (Drinovec et al., 2015), data in channel 6 (i.e., 880
 193 nm) can be used to retrieve M_{BC} .

195 2.2.3 VTDMA data analysis

196 The retrieved SF -PDF ($c(D_d, SF)$) is normalized as $\int c(D_d, SF) dSF = 1$. The ensemble mean
 197 shrink factor (SF_{mean}) is then calculated as

$$198 \quad SF_{\text{mean}}(D_d) = \int_0^{\infty} SF \cdot c(D_d, SF) dSF \quad (1)$$

199 Particles can be classified into several volatile groups according to different SF ranges (Y.
 200 Wang et al., 2017). The number fraction (NF) for each volatile group with the SF boundary of [a, b]
 201 is calculated as

$$202 \quad NF(D_d) = \int_a^b c(D_d, SF) dSF \quad (2)$$

203 Based on the core-shell assumption, the coating depth (D_c) of soot particles is defined as the
 204 depth of shell materials (i.e., shell depth). According to the definition of SF , D_c for the particle
 205 (D_d, SF) can be calculated as

$$206 \quad D_c(D_d, SF) = \frac{D_d}{2} (1 - SF) \quad (3)$$

207 The ensemble mean D_c ($D_{c,\text{mean}}$) using the normalized SF -PDF data is then calculated as

$$208 \quad D_{c,\text{mean}}(D_d) = \int_0^{\infty} D_c(D_d, SF) \cdot c(D_d, SF) dSF \quad (4)$$

210 3. Results and discussion

211 3.1 Meteorological conditions and aerosol pollution levels

212 Figure 1a-b shows the time series of ambient temperature (T), RH, and wind direction and
 213 speed (WD and WS, respectively) during the campaign. Monthly changes in T are clearly seen (Fig.
 214 2a). Average T s in warm (June, July, and August) and cold (May, September, and October) months
 215 were 25.73 ± 3.80 and $19.0 \pm 5.74^\circ\text{C}$, respectively. Figure 2a also suggests that RH was higher in July
 216 and August than in other months.

带格式的: 字体: (默认) Times New Roman

带格式的: 字体: (默认) Times New Roman

带格式的: 字体: (默认) Times New Roman

带格式的: 字体: (默认) Times New Roman, 五号, 字体颜色: 自定义颜色(RGB(0,0,204))

带格式的: 字体: (默认) Times New Roman, 五号, 字体颜色: 自定义颜色(RGB(0,0,204))

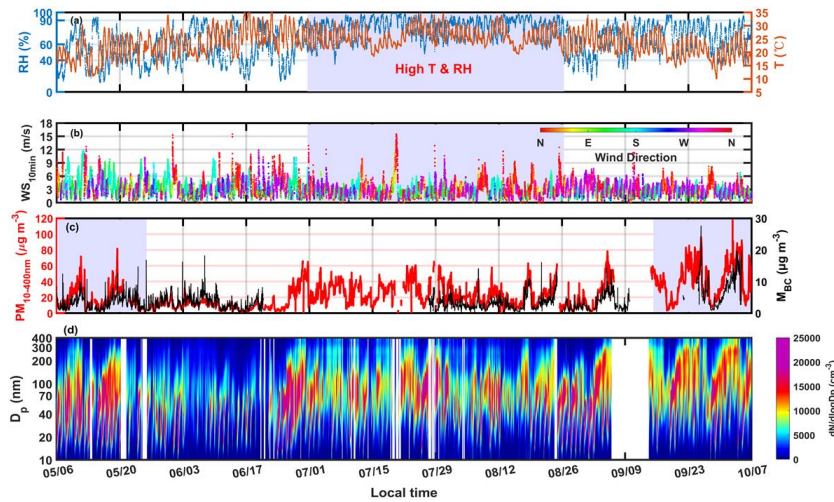
带格式的: 字体: 非倾斜, 字体颜色: 自定义颜色(RGB(0,0,204))

带格式的: 字体颜色: 自定义颜色(RGB(0,0,204)), 非上标/下标

带格式的: 字体颜色: 自定义颜色(RGB(0,0,204))

217 Figure 2b shows that the wind changed significantly in different months at XT. Monthly wind
 218 rose diagrams (Fig. S1) indicate that northwest winds prevailed in all months, likely caused by the
 219 special terrain around XT (Y. Zhang et al., 2018). In July, weak southeast winds were also
 220 present, beneficial to the accumulation of air pollutants due to the stable atmospheric
 221 environment. In August, the other prevailing wind was from the north, always strong and which was
 222 beneficial for atmospheric diffusion.

223



224

225 **Figure 2.** Time series of (a) ambient relative humidity (RH; unit: %), and temperature (T ; unit: °C),
 226 (b) wind direction (WD) and 10-minute-averaged wind speed (WS; unit: m s^{-1}), (c) mass
 227 concentration of 10–400 nm particles (PM_{10-400} , in red; unit: $\mu\text{g m}^{-3}$), assuming that the aerosol
 228 density is 1.6 g cm^{-3} , and mass concentration of black carbon (M_{BC} , in black; unit: $\mu\text{g m}^{-3}$), and (d)
 229 particle number size distribution at the Xingtai site from 6 May 2016 to 6 October 2016.

230

231 In this study, the total mass concentration of 10–400-nm particles (PM_{10-400}) (Fig. 2c) was
 232 calculated using PNSD data (Fig. 2d), assuming that the aerosol density was 1.6 g cm^{-3} (Y. Wang
 233 et al., 2017). The average PM_{10-400} concentrations in warm and cold months were 19.68 ± 13.58 and
 234 $29.79 \pm 21.37 \mu\text{g m}^{-3}$, respectively, indicating much higher aerosol pollution in cold months than in
 235 warm months. In cold months, PM_{10-400} accumulated periodically as accumulation-mode ($D_p > 100$
 236 nm) particles increased. This is closely related to cyclic changes in general atmospheric circulation,
 237 reflected by the cycle of winds (Fig. 2b). However, PM_{10-400} was lower in May than in September
 238 and October, likely due to the weaker particle growth in May. During warm months, PM_{10-400}
 239 reached its lowest value in June with the lowest number concentration of accumulation-mode
 240 particles of all months (Fig. S2), suggesting that meteorological conditions in June were not

241 conducive to particle growth. The high T and RH in July and August were beneficial to particle
242 growth by promoting atmospheric photochemical and liquid chemical reactions (Z. Wu et al., 2018;
243 Peng et al., 2021). Figure 2c suggests that PM_{10-400} was much higher in July and August than in June,
244 although the mass concentrations of black carbon (M_{BC}) in these months were considerable.
245 However, PM_{10-400} was lower in August than in July, likely because of the better atmospheric
246 diffusion conditions (more and stronger northerly winds) in August. Figure 2c also shows that
247 changes in M_{BC} and PM_{10-400} were similar, suggesting the possible non-trivial role of BC in the
248 formation processes of aerosol pollution. Recently, F. Zhang et al. (2020) demonstrated that BC-
249 catalyzed sulfate formation involving NO_2 and NH_3 plays an important role in the formation of haze
250 events.

251 ~~In summary, during the field campaign, meteorological conditions varied. Changes in~~
252 ~~meteorological parameters could influence the aging processes of particles, generating different~~
253 ~~aerosol pollution levels in different months. These changes would have a large impact on the~~
254 ~~volatility and mixing state of soot particles.~~

255

256 3.2 Monthly and diurnal variations in SF -PDF

257 Figure 3 shows ~~wavelength dependent, the~~ size-resolved mean SF -PDFs at XT. In general,
258 SF -PDFs had three peak modes, namely, at $SF \approx 0.4$ [very volatile (VV) mode], 0.6 [slightly
259 volatile (SV) mode], and 0.9 [nonvolatile (NV) mode]. The trimodal distributions of SF -PDFs at
260 XT in the central NCP differ from those at sites in the northern NCP (S. Zhang et al., 2016; Y.
261 Wang et al., 2017), implying highly complex volatility and mixing state of soot particles at XT.
262 Note that the SF -PDF of 40-nm particles has a quasi-unimodal distribution pattern, with low
263 fractions of NV- and SV-mode particles. Previous studies have indicated that most NV-mode
264 particles are externally mixed soot particles (Cheng et al., 2012; Cheung et al., 2016). This
265 suggests that soot-containing particles in nucleation mode (represented by 40-nm particles) in this
266 study had strong volatility and a high degree of internal mixing. Figure 3 also suggests that the
267 fraction of NV-mode particles increased with increasing particle size, indicating a higher fraction
268 of externally mixed soot particles in accumulation mode. This is related to the primary size of soot
269 particles. Some studies suggest that freshly emitted refractory particles (like BC) are primarily in
270 accumulation mode. For example, Levy et al. (2013) reported that fresh BC was mostly in the
271 150–240 nm size range, while Wu et al. (2017) reported that refractory BC size distribution
272 measurements in Beijing peaked at about 200 nm, with a secondary less significant mode at about
273 600 nm. Levy et al. (2014) and Wu et al. (2017) have suggested that freshly emitted refractory-
274 particles (like BC) are primarily in accumulation mode.

275

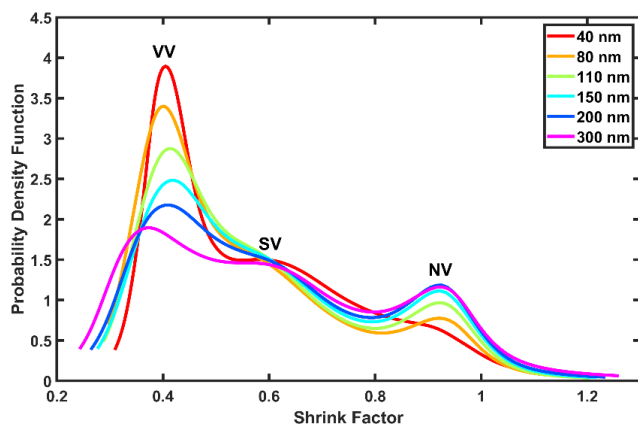
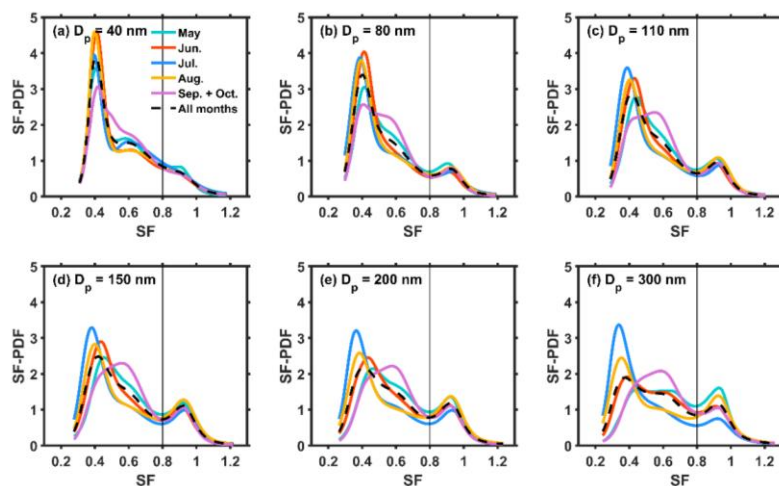


Figure 3. Size-resolved mean probability density functions of the shrink factor at different wavelengths. VV stands for “very volatile”, SV stands for “slightly volatile”, and NV stands for “non-volatile”.

Figure 4a-b shows that VV-mode fractions in the *SF*-PDFs of 40-nm and 80-nm particles were higher in warm months than in cold months, indicating that nucleation-mode soot particles were more volatile in warm months. Our previous study has shown that new particle formation (NPF) events occurred frequently at XT (Y. Wang et al., 2018). Wehner et al. (2009) reported that most newly formed matter is composed of organics and sulfate, easily volatilized at 300°C. All this implies that coating by newly formed secondary matter was the possible reason for the high volatility of nucleation-mode soot-containing particles in warm months. For accumulation-mode (110–300 nm) particles (Fig. 4c-f), monthly changes in *SF*-PDF patterns are clearly seen. In general, *SF* peak values of the VV mode were smaller (meaning a thicker coating of volatile matter), and fractions of VV-mode particles were higher in warm months (especially in July) than in cold months, indicating that the coating on accumulation-mode soot particles was also stronger in warm months than in cold months. As previously mentioned, meteorological conditions in warm months (i.e., high *T* and RH) were favorable to the particle growth of soot particles through atmospheric photochemical and liquid chemical reactions. In cold months (May, September, and October), the volatility of accumulation-mode soot-containing particles was relatively lower, indicating thinner coating matter on the surfaces of soot particles in the polluted cold environment. This is consistent with measurements made at an urban site in Beijing (Yu et al., 2020; Wang et al., 2017). Yu et al. (2020) also suggests that a more even distribution of γ BC and non- γ BC material mass fractions in summer than in winter, which may be caused by higher amount of secondary material.

带格式的: 字体: 倾斜

带格式的: 字体: 倾斜



301

302 **Figure 4.** Monthly variations in the mean shrink factor (SF) probability distribution functions (SF -
 303 PDFs) for particles with diameters of (a) 40 nm, (b) 80 nm, (c) 110 nm, (d) 150 nm, (e) 200 nm,
 304 and (f) 300 nm.

305

306

307

308

309

310

311

312

313

314

315

316

317

318

319

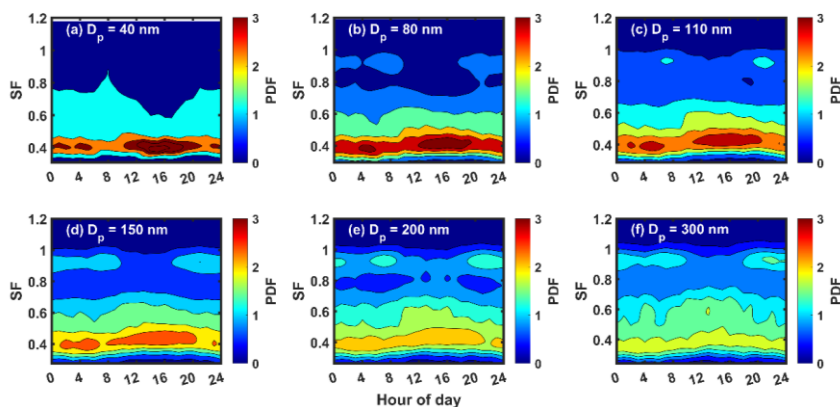
320

321

322

323

Figure 5 shows diurnal variations in SF -PDF for different size particles, illustrating the distinct diurnal variation patterns of SF -PDF for nucleation- and accumulation-mode particles. VV-mode fractions for 40-nm and 80-nm particles ($\sim SF = 0.4$) increased sharply from around noon into the afternoon (Fig. 5a-b). Figure S3 shows that the number concentration of 40-nm and 80-nm particles increased quickly due to the influence of NPF events. This further corroborates that newly formed particles created during NPF events are the possible coating matter on nucleation-mode soot particles. Figure 5c-f suggests that NV-mode fractions in accumulation-mode soot particles ($\sim SF = 0.9$) were higher than those in nucleation-mode soot particles and that these fractions became higher with increasing particle size. NV-mode fractions in accumulation-mode soot particles clearly increased during the morning and evening rush hours. This suggests that anthropogenic emissions have a large impact on the volatility and mixing state of soot particles, especially for accumulation-mode soot particles. Previous studies have shown that some of the primary pollutants generated by human activities are composed of refractory materials, such as BC (Philippin et al., 2004; Levy et al., 2014). An increase in primary refractory particles could weaken the ensemble volatility and mixing state of soot particles. Figure 3c-f also shows that the NV-mode fraction in the SF -PDF of accumulation-mode particles decreased sharply in the daytime, likely caused by the coating effect of volatile matter through photochemical reactions.



324

325 **Figure 5.** Diurnal variations in size-resolved shrink factor (SF) probability distribution functions
 326 (PDFs) for particles with diameters of (a) 40 nm, (b) 80 nm, (c) 110 nm, (d) 150 nm, (e) 200 nm,
 327 and (f) 300 nm.

328

329 In summary, the volatility and mixing state of soot-containing particles were complex at XT
 330 during the field campaign. Soot-containing particles in the nucleation mode had strong volatility
 331 and a high degree of internal mixing, likely due to the impact of frequent NPF events that occurred
 332 during this campaign. The strong volatility and high degree of internal mixing in warm months were
 333 likely caused by the aging processes of particles. Anthropogenic emissions also had a large impact
 334 on the volatility and mixing state of soot particles, especially in the accumulation mode. The impacts
 335 of anthropogenic emissions and secondary chemical reactions on the volatility and mixing state of
 336 soot particles will be further discussed next.

337

338 3.3 Factors influencing the volatility and mixing state of soot particles

339 3.3.1 The impact of anthropogenic emissions on the volatility and mixing state of soot 340 particles

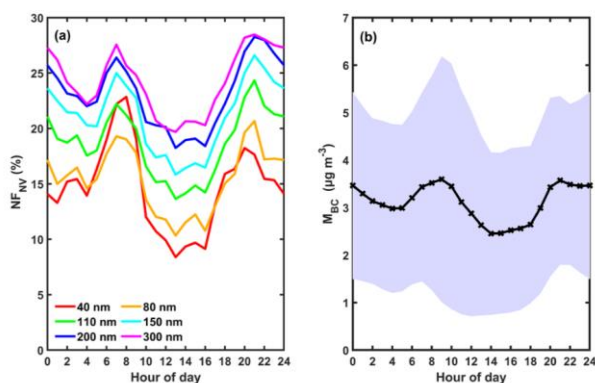
341 As previously discussed, soot particles from anthropogenic emissions were always refractory
 342 and nonvolatile at 300°C. Analyzing the relationship between the number fraction of nonvolatile-
 343 mode particles (NF_{NV} , $SF > 0.8$) in SF -PDFs and M_{BC} can verify this because BC is the main matter
 344 in soot particles. Figure 6a shows that NF_{NV} reached two peak values, one during the morning rush
 345 hour at about 08:00 and the other during the evening rush hour at about 20:00. M_{BC} also reached
 346 two peak values at those same times (Fig. 6b). Overall, the diurnal variation trends of NF_{NV} for all
 347 sizes and M_{BC} were similar. This suggests the great impact of anthropogenic BC on the volatility
 348 and mixing state of soot particles. NF_{NV} decreased quickly after rush hours, especially in the

349 morning (Fig. 6a), suggesting that the aging processes of primary soot particles were quick at this
350 heavily polluted site. [Cheng et al. \(2012\)](#) also observed the same phenomenon at a suburban site in
351 [Beijing](#).

带格式的: 字体颜色: 自动设置

带格式的: 字体颜色: 自动设置

带格式的: 缩进: 首行缩进: 0 字符

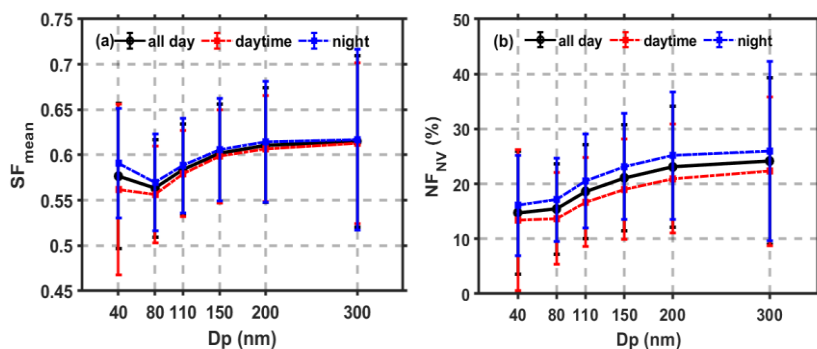


353 **Figure 6.** Diurnal variations in (a) wavelength-dependent, size-resolved number fractions of
354 nonvolatile particles (NF_{NV}), and (b) mass concentration of black carbon (M_{BC}). The purple,
355 shaded area shows the standard deviations of M_{BC} .
356

357
358 3.3.2 The impact of aging processes on the volatility and mixing state of soot-containing
359 particles

360 Lower SF_{mean} values mean stronger aerosol volatility, indicating a larger coating depth of volatile
361 matter on soot particles. Figure 7a suggests that volatility is stronger during daytime than at night
362 (i.e., a lower SF_{mean}), particularly for 40-nm particles. This illustrates the large impact of
363 photochemical reactions on the volatility and mixing state of soot particles. [Figure 7a also suggests](#)
364 [that the \$SF_{\text{mean}}\$ of 80-nm particles was lower than that of 40-nm particles, meaning that the](#)
365 [volatility of nucleation-mode soot particles became larger with increasing particle size.](#) [Wang et al.](#)
366 [\(2018\) suggests that aerosol hygroscopicity of 40-nm particles is larger than that of 80-nm particles](#)
367 [during the daytime at this site. These indicate the great impact of photochemical reactions on the](#)
368 [physicochemical properties of nucleation-mode particles.](#) Inversely, SF_{mean} increased with
369 increasing particle size in the accumulation mode (110–300 nm), suggesting weaker volatility and
370 a smaller coating depth for larger accumulation-mode soot particles.

371



372
 373 **Figure 7.** (a) Size-resolved ensemble mean shrink factors (SF_{mean}) and (b) size-resolved number
 374 fractions of nonvolatile particles (NF_{NV}) during the 24-hr day (black solid lines), during daytime
 375 (red dotted lines), and during nighttime (blue dotted lines). The error bars denote standard deviations.

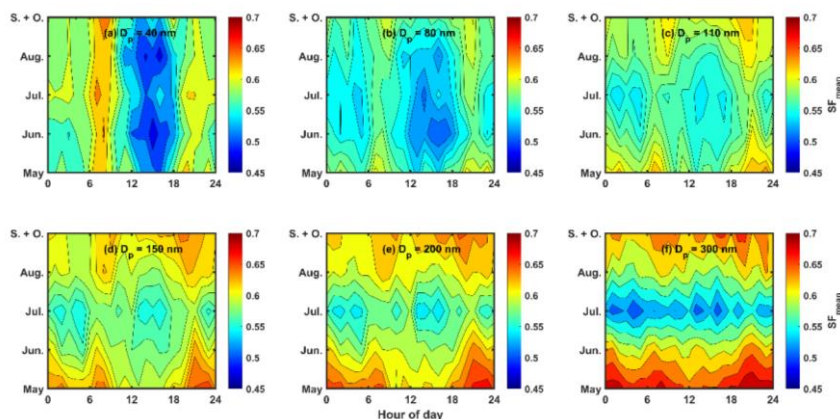
376 Figure 8 shows the diurnal variation in SF_{mean} in different months for different particle sizes.
 377 Figure 8a-b shows that the SF_{mean} of 40-nm and 80-nm particles clearly increased during the
 378 morning and evening rush hours in all months. However, the SF_{mean} of 40-nm and 80-nm particles
 379 decreased sharply in the afternoon. This suggests that the volatility of nucleation-mode soot-
 380 containing particles was easily influenced by anthropogenic emissions during rush hours and
 381 photochemical reactions in the daytime. The diurnal variation patterns of SF_{mean} (Fig. 8c-f) in the
 382 accumulation mode were diverse in different months. The SF_{mean} in warm months was usually lower
 383 than in cold months, indicating a larger impact of aging processes on the volatility of accumulation-
 384 mode soot-containing particles in warm months. Figure 8c-f also shows that the SF_{mean} in
 385 accumulation mode was lowest in July. This suggests that high T , high RH, and the stable
 386 atmospheric environment in July were conducive to the coating of secondary matter on
 387 accumulation-mode soot particles, a possible reason for the high aerosol pollution levels in July.
 388 Moreover, Fig. 8 suggests that monthly variations in SF_{mean} became larger with increasing particle
 389 size. The seasonal variation in the coating effect should thus be considered when modeling
 390 physicochemical properties of soot particles, especially larger particles.

391 To further investigate the impact of aging processes on the mixing state of soot particles, size-
 392 resolved NF_{NV} in the daytime and at night were compared (Fig. 7b). NF_{NV} was always lower in the
 393 daytime than at night, meaning that the fraction of externally mixed soot particles in the daytime
 394 was lower. This further indicates that photochemical reactions in the daytime can transform
 395 externally mixed soot particles into internally mixed soot particles. Figure 7b also shows that NF_{NV}
 396 increased with increasing particle size, meaning a higher degree of external mixing of larger
 397 particles. This suggests that the degree of external mixing was higher for accumulation-mode soot
 398 particles than nucleation-mode particles.

399 The diurnal variation patterns of NF_{NV} (Fig. S4) and SF_{mean} (Fig. 8) in different months were
 400 similar. Externally mixed soot particles increased during the morning and evening rush hours due
 401 to enhanced anthropogenic emissions. Monthly differences in NF_{NV} increased with increasing
 402 particle size. Figure S4 also shows a lower number fraction of externally mixed soot particles (i.e.,
 403 a smaller NF_{NV}) in warm months than in cold months.

404 These results illustrate the distinct volatilities and mixing states of soot particles between the
 405 nucleation and accumulation modes. A lower degree of external mixing and thicker coating depth
 406 in nucleation-mode particles exists. It is thus important to quantify the impact of the coating effect
 407 for nucleation-mode soot particles when studying aerosol physicochemical properties. The next
 408 section analyzes the coating depth and its influencing factors.

409



410

411

412

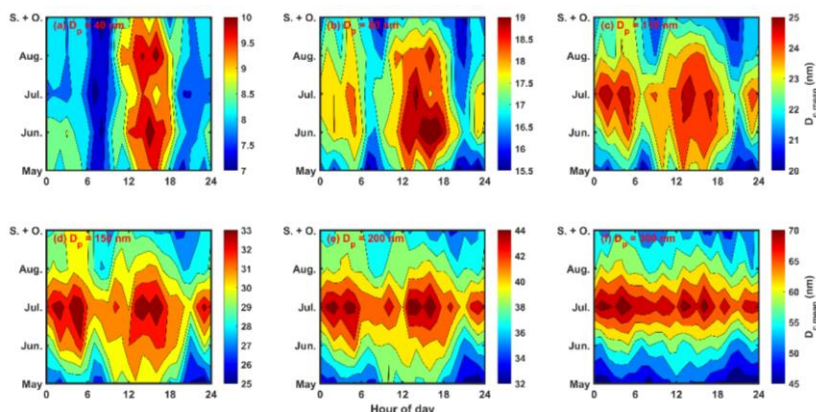
Figure 8. Diurnal variations in ensemble mean shrink factor (SF_{mean}) in different months for different particle sizes.

413

414 3.4 The coating depth of secondary matter on soot particles

415 The ensemble mean coating depth on soot particles ($D_{c,mean}$) can be calculated using Eq. (4).
 416 Figure 9 shows diurnal variations in $D_{c,mean}$ in different months for different particle sizes. The
 417 diurnal variation patterns of $D_{c,mean}$ for nucleation-mode and accumulation-mode soot particles
 418 differ greatly. The diurnal variation patterns of $D_{c,mean}$ in different months were similar for
 419 nucleation-mode soot particles (40-nm and 80-nm particles) but not for accumulation-mode soot
 420 particles (110–300-nm particles). The enhancement of $D_{c,mean}$ in the daytime occurred in all months
 421 for nucleation-mode soot particles but only in the warm months for accumulation-mode soot
 422 particles. At night, the enhancement of $D_{c,mean}$ for accumulation-mode soot particles was strong,
 423 especially in warm months. However, it was weak for nucleation-mode soot particles. These all

424 imply large differences in $D_{c,mean}$ in different months for nucleation-mode and accumulation-mode
 425 soot particles, likely caused by variations in meteorological conditions and aerosol pollution levels.
 426



427
 428 **Figure 9.** Diurnal variations in ensemble mean coating depth ($D_{c,mean}$) on soot particles in different
 429 months for different particle sizes. Note that the color bars have different ranges of values in each
 430 panel.
 431

432 The relationships between $D_{c,mean}$ and several possible influencing factors (T , RH, and $PM_{10-400nm}$)
 433 were further analyzed (Fig. 10). Figures 10a and 10d show positive correlations between
 434 $D_{c,mean}$ and T for both nucleation-mode and accumulation-mode particles (represented by 40-nm and
 435 300-nm particles, respectively). This is consistent with the results shown in Fig. 7. Zhang et al.
 436 (2021) also indicated that warm environments were favorable to the aging of γ BC. The high daytime
 437 T was conducive to the aging of soot particles-likely caused by strong photochemical reactions.
 438 However, the relationships between RH and $D_{c,mean}$ (Figs. 9b and 9e) and between $PM_{10-400nm}$ and
 439 $D_{c,mean}$ (Figs. 9c and 9f) were inverse between nucleation- and accumulation-mode soot particles.

440 Figure 9 depicts a linear relationship between $D_{c,mean}$ and RH, while a logarithmic relationship
 441 between $D_{c,mean}$ and $PM_{10-400nm}$. $D_{c,mean}$ in the nucleation mode decreased with increasing RH and
 442 $PM_{10-400nm}$ for nucleation-mode soot particles (Fig. 9b-c). This suggests that high ambient RH and
 443 severe aerosol pollution events could inhibit the coating of nucleation-mode soot particles. Previous
 444 studies have reported that aerosol pollution events were generally associated with high RH in the
 445 NCP (G. Wang et al., 2016; Z. Wu et al., 2018). This suggests that highly polluted environments
 446 with high ambient RH are not beneficial to the formation of new particles, leading to the weak
 447 coating on nucleation-mode soot particles. However, $D_{c,mean}$ in the accumulation mode increased
 448 with increasing RH and $PM_{10-400nm}$ (Fig. 9e-f). This suggests that highly polluted environments with
 449 high ambient RH favor the growth of accumulation-mode soot particles by coating. This is possibly

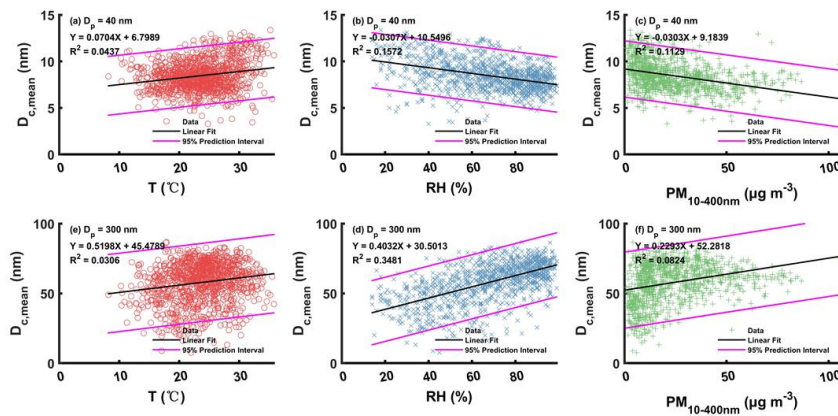
带格式的: 字体: 倾斜

带格式的: 字体颜色: 自动设置

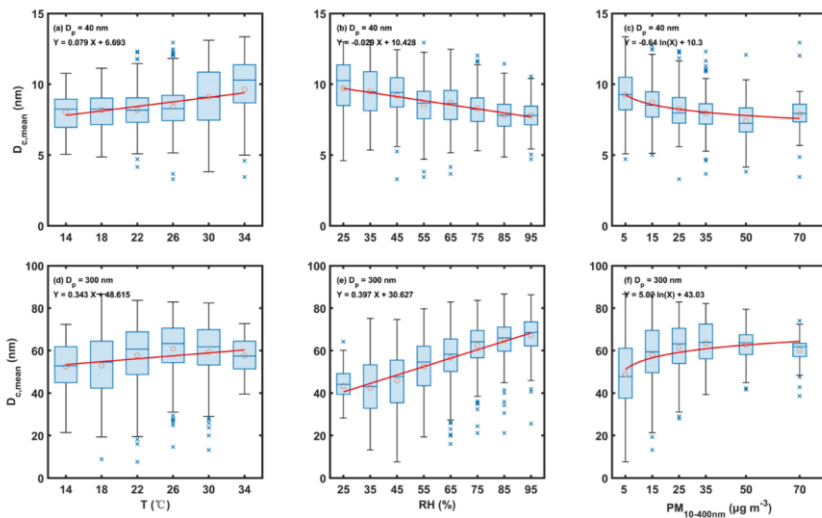
450 related to enhanced liquid-phase chemical reactions under these environmental conditions.
 451 Considering that accumulation-mode particles are the dominant components of $PM_{10-400nm}$, this
 452 further implies that the coating on soot particles is important to the formation of heavy aerosol
 453 pollution events. [Y. Wang et al. \(2019\)](#) indicated that the properties of ultrafine- and accumulation-
 454 mode particles were distinct in clean and polluted urban environments due to the different particle
 455 formation and growth processes. This study further indicates that it is also distinct in the aging of
 456 soot particles.

457 In summary, high ambient T and RH levels appeared to promote the coating growth of
 458 accumulation-mode soot particles in highly polluted environments. High ambient T but low RH
 459 were beneficial to the coating growth of nucleation-mode soot particles in less polluted
 460 environments.

461



462



463

464 **Figure 10.** Relationships between ensemble mean coating depth ($D_{c,mean}$) and ambient T (a, d) and
 465 RH (b, e), and $PM_{10-400nm}$ (c, f) for 40-nm (top panels) and 300-nm (bottom panels) particles.
 466 The black lines show the linear best-fit lines through the data, circles show the mean $D_{c,mean}$ with
 467 boxes showing the 25th, 50th, and 75th percentiles and extremities show the 5th and 95th percentiles.
 468 Red lines show the linear or logarithmic fitting lines through the data, and magenta lines show
 469 the 95% prediction levels. Linear best-fit relations and coefficients of determination are given in
 470 each panel.

471

472 4. Summary and conclusions

473 Soot particles containing most of the black carbon (BC) in the atmosphere are the most
 474 important light-absorbing carbonaceous particles. Investigating the mixing state of soot particles in
 475 the field is crucial to accurately model aerosol absorption and reduce the uncertainty of radiative
 476 forcing caused by aerosols in climate models.

477 Here, over five months of volatility tandem differential mobility analyzer (VTDMA) data
 478 collected at a heavily polluted suburban site (Xingtai, or XT) from May to October of 2016 were
 479 used to study the volatility and mixing state of size-resolved soot particles and their influencing
 480 factors. Ambient meteorological variables [temperature (T), relative humidity (RH), and winds]
 481 varied between the warm (June, July, and August) and cold (May, September, and October) months
 482 of the field campaign. Variations in meteorological parameters could induce various aerosol aging
 483 processes and different levels of aerosol pollution, largely impacting the volatility and mixing state
 484 of soot particles.

带格式的: 字体: (默认) Times New Roman, 五号
 带格式的: 字体: (默认) Times New Roman, 五号
 带格式的: 字体: (默认) Times New Roman, 五号
 带格式的: 字体: (默认) Times New Roman, 五号

485 The retrieved probability density function of the shrink factor (SF -PDF) at XT had three modes,
486 demonstrating that the volatility and mixing state of soot-containing particles were more complex
487 at XT than at other sites in the North China Plain. Compared with accumulation-mode soot particles,
488 nucleation-mode soot-containing particles were more volatile and had a higher degree of internal
489 mixing. The diurnal variation patterns of SF -PDFs suggest that coating by newly formed
490 materials particles was the possible reason for the enhanced volatility of nucleation-mode soot-
491 containing particles in the daytime. Moreover, the enhanced nocturnal secondary aerosol formation
492 ~~nocturnal liquid chemical reactions were was~~ responsible for the enhanced volatility of
493 accumulation-mode soot-containing particles in the nighttime. The ensemble mean SF (SF_{mean}) was
494 size dependent and varied monthly. The monthly variations in SF_{mean} became larger with increasing
495 particle size, implying a stronger seasonal variation of the coating effect on soot particles for larger-
496 sized particles.

497 The similar diurnal variation trends of the number fraction of nonvolatile mode particles (NF_{NV})
498 in SF -PDFs and the mass concentration of BC (M_{BC}) suggest that human activities had a negative
499 influence on the volatility and degree of internal mixing of soot particles, especially for
500 accumulation-mode soot-containing particles. In general, less externally mixed soot particles (i.e.,
501 a smaller NF_{NV}) were present in warm months than in cold months. NF_{NV} was always lower in the
502 daytime than at night, suggesting a lower fraction of externally mixed soot particles in the daytime.
503 This suggests that daytime photochemical reactions may promote the transformation of externally
504 mixed soot particles into internally mixed soot particles. Moreover, NF_{NV} increased with increasing
505 particle size, meaning a higher degree of external mixing for larger-sized particles. This also
506 suggests that the degree of external mixing was higher for accumulation-mode soot particles than
507 for nucleation-mode soot particles.

508 To explore factors influencing soot-particle volatility and mixing state, the ensemble mean
509 coating depth ($D_{\text{c,mean}}$) of volatile matter on soot particles was investigated. $D_{\text{c,mean}}$ was thicker in
510 warm months than in cold months, even though aerosol pollution was heavier in cold months. In
511 warm months, $D_{\text{c,mean}}$ was larger in July than in other months, likely because high T , high RH, and
512 the stable atmospheric environment in July were conducive to the coating effect on soot particles.
513 The relationships between $D_{\text{c,mean}}$ and possible influencing factors (i.e., T , RH, and $\text{PM}_{10-400\text{nm}}$) show
514 that high ambient T and RH in a polluted environment promoted the coating growth of
515 accumulation-mode soot particles. High ambient T but low RH in a clean environment was
516 beneficial to the coating growth of nucleation-mode soot particles.

517 These results demonstrate great differences in the volatility and mixing state between nucleation-
518 and accumulation-mode soot particles. The impact of anthropogenic emissions on the volatility and
519 mixing state of soot-containing particles was clearly seen, especially for accumulation-mode soot-

520 containing particles. The monthly variations in meteorological conditions and aerosol pollution
521 levels may induce different aerosol aging processes, strongly impacting the volatility and mixing
522 state of soot-containing particles. This study suggests that differences between the mixing states of
523 nucleation- and accumulation-mode soot particles and their influencing factors should be considered
524 in climate models.

525
526 *Acknowledgement.* This work was funded by the National Natural Science Foundation of China
527 (NSFC) research project (grant no. 42030606, 42005067, 92044303), the National Key R&D
528 Program of the Ministry of Science and Technology, China (grant no. 2017YFC1501702), and the
529 Open Fund of State Key Laboratory of Remote Sensing Science (grant no. 202015). We also thank
530 all participants in the campaign for their tireless work and cooperation.

531
532 *Data availability.* The measurement data from the field experiment used in this study are available
533 from the first author upon request (yuyingwang@nuist.edu.cn).

534
535 *Author contributions.* YW conceived the study and led the overall scientific questions. YW,
536 RH, and QW processed the measurement data and prepared this paper. ZL, MC copyedited the
537 article. Other co-authors participated in the implementation of this experiment and the discussion
538 of this paper.

539
540 *Competing interests.* The authors declare that they have no conflict of interest.

541
542
543

544 **References**

545 Adachi, K., Sedlacek, A. J., Kleinman, L., Chand, D., Hubbe, J. M., and Buseck, P. R.: Volume changes
546 upon heating of aerosol particles from biomass burning using transmission electron microscopy,
547 Aerosol Sci. Tech., 52, 46-56, <https://doi.org/10.1080/02786826.2017.1373181>, 2018.
548 Adachi, K., Sedlacek, A. J., Kleinman, L., Springston, S. R., Wang, J., Chand, D., Hubbe, J. M., Shilling,
549 J. E., Onasch, T. B., Kinase, T., Sakata, K., Takahashi, Y., and Buseck, P. R.: Spherical tarball
550 particles form through rapid chemical and physical changes of organic matter in biomass-burning
551 smoke. Proceedings of the National Academy of Sciences, 116, 19336-19341,
552 <https://doi.org/10.1073/pnas.1900129116>, 2019.
553 Bellouin, N., Quaas, J., Gryspeerdt, E., Kinne, S., Stier, P., Watson-Parris, D., Boucher, O., Carslaw, K.

带格式的: 字体: (默认) Times New Roman, (中文) + 中文正文 (等线), 10 磅, 英语(美国)

带格式的: 字体: (默认) Times New Roman, (中文) + 中文正文 (等线), 10 磅, 英语(美国)

带格式的: 字体: (默认) Times New Roman, (中文) + 中文正文 (等线), 10 磅, 英语(美国)

带格式的: 字体: (默认) Times New Roman, (中文) + 中文正文 (等线), 10 磅, 英语(美国)

554 S., Christensen, M., Daniau, A. L., Dufresne, J. L., Feingold, G., Fiedler, S., Forster, P., Gettelman,
555 A., Haywood, J. M., Lohmann, U., Malavelle, F., Mauritsen, T., McCoy, D. T., Myhre, G.,
556 Mülmenstädt, J., Neubauer, D., Possner, A., Rugenstein, M., Sato, Y., Schulz, M., Schwartz, S. E.,
557 Sourdeval, O., Storelvmo, T., Toll, V., Winker, D., and Stevens, B.: Bounding global aerosol radiative
558 forcing of climate change, *Rev. Geophys.*, 58, e2019R-e2660R, 2020.

559 Bond, T. C., Doherty, S. J., Fahey, D. W., Forster, P. M., Berntsen, T., DeAngelo, B. J., Flanner, M. G.,
560 Ghan, S., Kärcher, B., Koch, D., Kinne, S., Kondo, Y., Quinn, P. K., Sarofim, M. C., Schultz, M. G.,
561 Schulz, M., Venkataraman, C., Zhang, H., Zhang, S., Bellouin, N., Guttikunda, S. K., Hopke, P. K.,
562 Jacobson, M. Z., Kaiser, J. W., Klimont, Z., Lohmann, U., Schwarz, J. P., Shindell, D., Storelvmo, T.,
563 Warren, S. G., and Zender, C. S.: Bounding the role of black carbon in the climate system: A scientific
564 assessment, *J. Geophys. Res. Atmos.*, 118, 5380-5552, <https://doi.org/10.1002/jgrd.50171>, 2013.

565 Cheng, Y. F., Berghof, M., Garland, R. M., Wiedensohler, A., Wehner, B., Müller, T., Su, H., Zhang, Y.
566 H., Achtert, P., Nowak, A., Pöschl, U., Zhu, T., Hu, M., and Zeng, L. M.: Influence of soot mixing
567 state on aerosol light absorption and single scattering albedo during air mass aging at a polluted
568 regional site in northeastern China, *J. Geophys. Res. Atmos.*, 114, 2009.

569 Cheng, Y. F., Su, H., Rose, D., Gunthe, S. S., Berghof, M., Wehner, B., Achtert, P., Nowak, A.,
570 Takegawa, N., Kondo, Y., Shiraiwa, M., Gong, Y. G., Shao, M., Hu, M., Zhu, T., Zhang, Y. H.,
571 Carmichael, G. R., Wiedensohler, A., Andreae, M. O., and Pöschl, U.: Size-resolved measurement of
572 the mixing state of soot in the megacity Beijing, China: diurnal cycle, aging and parameterization,
573 *Atmos. Chem. Phys.*, 12, 4477-4491, 2012.

574 Cheung, H. H., Tan, H., Xu, H., Li, F., Wu, C., Yu, J. Z., and Chan, C. K.: Measurements of non-volatile
575 aerosols with a VTDMA and their correlations with carbonaceous aerosols in Guangzhou, China,
576 *Atmos. Chem. Phys.*, 16, 8431-8446, 2016.

577 Christensen, M., Gettelman, A., Cermak, J., Dagan, G., Diamond, M., Douglas, A., Feingold, G.,
578 Glassmeier, F., Goren, T., Grosvenor, D., Gryspeerd, E., Kahn, R., Li, Z., Ma, P. L., Malavelle, F.,
579 McCoy, I., McCoy, D., McFarquhar, G., Mülmenstädt, J., Pal, S., Possner, A., Povey, A., Quaas, J.,
580 Rosenfeld, D., Schmidt, A., Schrödner, R., Sorooshian, A., Stier, P., Toll, V., Watson-Parris, D.,
581 Wood, R., Yang, M., and Yuan, T.: Opportunistic experiments to constrain aerosol effective radiative
582 forcing, *Atmos. Chem. Phys. Discuss.*, 2021, 1-60, 2021.

583 Gustafsson, Ö., and Ramanathan, V.: Convergence on climate warming by black carbon aerosols, *Proc.*
584 *Natl. Acad. Sci. U.S.A.*, 113, 4243, <https://doi.org/10.1073/pnas.1603570113>, 2016.

585 Hong, J., Äijälä, M., Häme, S. A. K., Hao, L., Duplissy, J., Heikkinen, L. M., Nie, W., Mikkilä, J.,
586 Kulmala, M., Prisle, N. L., Virtanen, A., Ehn, M., Paasonen, P., Worsnop, D. R., Riipinen, I., Petäjä,
587 T., and Kerminen, V. M.: Estimates of the organic aerosol volatility in a boreal forest using two
588 independent methods, *Atmos. Chem. Phys.*, 17, 4387-4399, [https://doi.org/10.5194/acp-17-4387-](https://doi.org/10.5194/acp-17-4387-2017)
589 2017, 2017.

590 Hossain, A. M. M., Park, S., Kim, J. S., and Park, K.: Volatility and mixing states of ultrafine particles
591 from biomass burning, *J. Hazard. Mater.*, 205-206, 189-197, 2012.

592 IPCC: Climate change 2021: The Physical Science Basis, sixth assessment of the Inter-governmental
593 Panel on Climate Change, in press, 2021.

594 Kuniyal, J. C., and Guleria, R. P.: The current state of aerosol-radiation interactions: a mini review, *J.*
595 *Aerosol Sci.*, 130, 45-54, 2019.

596 [Levy, M. E., Zhang, R., Khalizov, A. F., Zheng, J., Collins, D. R., Glen, C. R., Yuan, W., Yu, X. Y.,](#)
597 [Winston, L., and Jayne, J. T.: Measurements of submicron aerosols in Houston, Texas during the 2009](#)

598 [SHARP field campaign, J. Geophys. Res. Atmos., 118, 10.518-10.534,](#)
599 <https://doi.org/10.1002/jgrd.50785>, 2013.

600 Levy, M. E., Zhang, R., Zheng, J., Tan, H., Wang, Y., Molina, L. T., Takahama, S., Russell, L. M., and
601 Li, G.: Measurements of submicron aerosols at the California - Mexico border during the Cal-Mex
602 2010 field campaign, *Atmos. Environ.*, 88, 308-319, 2014.

603 Li, Z., Wang, Y., Guo, J., Zhao, C., Cribb, M. C., Dong, X., Fan, J., Gong, D., Huang, J., Jiang, M., Jiang,
604 Y., Lee, S. S., Li, H., Li, J., Liu, J., Qian, Y., Rosenfeld, D., Shan, S., Sun, Y., Wang, H., Xin, J., Yan,
605 X., Yang, X., Yang, X., Zhang, F., and Zheng, Y.: East Asian Study of Tropospheric Aerosols and
606 their Impact on Regional Clouds, Precipitation, and Climate (EAST-AIR_{CPC}), *J. Geophys. Res.*
607 *Atmos.*, 124, 13,026-13,054, <https://doi.org/10.1029/2019JD030758>, 2019.

608 [Drinovec, L., Močnik, G., Zotter, P., Prévôt, A. S. H., Ruckstuhl, C., Coz, E., Rupakheti, M., Sciare, J.,](#)
609 [Müller, T., Wiedensohler, A., and Hansen, A. D. A.: The "dual-spot" Aethalometer: an improved](#)
610 [measurement of aerosol black carbon with real-time loading compensation, Atmos. Meas. Tech., 8,](#)
611 [1965-1979, https://doi.org/10.5194/amt-8-1965-2015](https://doi.org/10.5194/amt-8-1965-2015).

612 Novakov, T., Ramanathan, V., Hansen, J. E., Kirchstetter, T. W., Sato, M., Sinton, J. E., and Sathaye, J.
613 A.: Large historical changes of fossil-fuel black carbon aerosols, *Geophys. Res. Lett.*, 30,
614 <https://doi.org/10.1029/2002GL016345>, 2003.

615 Peng, J., Hu, M., Guo, S., Du, Z., Zheng, J., Shang, D., Zamora, M. L., Zeng, L., Shao, M., and Wu, Y.:
616 Markedly enhanced absorption and direct radiative forcing of black carbon under polluted urban
617 environments, *Proc. Natl. Acad. Sci. U.S.A.*, 113, 4266-4271, 2016.

618 Peng, J., Hu, M., Shang, D., Wu, Z., Du, Z., Tan, T., Wang, Y., Zhang, F., and Zhang, R.: Explosive
619 secondary aerosol formation during severe haze in the North China Plain, *Environ. Sci. Technol.*, 55,
620 2189-2207, <https://doi.org/10.1021/acs.est.0c07204>, 2021.

621 Philippin, S., Wiedensohler, A., and Stratmann, F.: Measurements of non-volatile fractions of pollution
622 aerosols with an eight-tube volatility tandem differential mobility analyzer (VTDMA-8), *J. Aerosol*
623 *Sci.*, 35, 185-203, <https://doi.org/10.1016/j.jaerosci.2003.07.004>, 2004.

624 Ramana, M. V., Ramanathan, V., Feng, Y., Yoon, S., Kim, S., Carmichael, G. R., and Schauer, J. J.:
625 Warming influenced by the ratio of black carbon to sulphate and the black-carbon source, *Nat. Geosci.*,
626 3, 542-545, <https://doi.org/10.1038/ngeo918>, 2010.

627 Ren, R., Li, Z., Yan, P., Wang, Y., Wu, H., Cribb, M., Wang, W., Jin, X., Li, Y., and Zhang, D.:
628 Measurement report: the effect of aerosol chemical composition on light scattering due to the
629 hygroscopic swelling effect, *Atmos. Chem. Phys.*, 21, 9977-9994, 2021.

630 Seinfeld, J. H., Bretherton, C., Carslaw, K. S., Coe, H., DeMott, P. J., Dunlea, E. J., Feingold, G., Ghan,
631 S., Guenther, A. B., Kahn, R., Kraucunas, I., Kreidenweis, S. M., Molina, M. J., Nenes, A., Penner, J.
632 E., Prather, K. A., Ramanathan, V., Ramaswamy, V., Rasch, P. J., Ravishankara, A. R., Rosenfeld,
633 D., Stephens, G., and Wood, R.: Improving our fundamental understanding of the role of aerosol-
634 cloud interactions in the climate system, *Proc. Natl. Acad. Sci. U.S.A.*, 113, 5781, 2016.

635 Stolzenburg, M. R., and McMurry, P. H.: TDMAFIT user's manual, University of Minnesota,
636 Department of Mechanical Engineering, Particle Technology Laboratory, Minneapolis, 1-61, 1988.

637 Stolzenburg, M. R., and McMurry, P. H.: Equations governing single and tandem DMA configurations
638 and a new lognormal approximation to the transfer function, *Aerosol Sci. Tech.*, 42, 421-432, 2008.

639 Swietlicki, E., Hansson, H. C., Hämeri, K., Svenningsson, B., Massling, A., Mcfiggans, G., McMurry, P.
640 H., Petäjä, T., Tunved, P., Gysel, M., Topping, D., Weingartner, E., Baltensperger, U., Rissler, J.,

带格式的: 字体: (默认) Times New Roman, 10 磅, 字体颜色: 黑色

带格式的: 字体: (默认) Times New Roman, 10 磅, 字体颜色: 黑色

641 Wiedensohler, A., and Kulmala, M.: Hygroscopic properties of submicrometer atmospheric aerosol
 642 particles measured with H-TDMA instruments in various environments—a review, *Tellus B: Chem.*
 643 *Phys. Meteor.*, 60, 432-469, <https://doi.org/10.1111/j.1600-0889.2008.00350.x>, 2008.

644 Twohy, C. H., Coakley Jr., J. A., and Tahnk, W. R.: Effect of changes in relative humidity on aerosol
 645 scattering near clouds, *J. Geophys. Res. Atmos.*, 114, 2009.

646 Wang, G., Zhang, R., Gomez, M. E., Yang, L., Zamora, M. L., Hu, M., Lin, Y., Peng, J., Guo, S., and
 647 Meng, J.: Persistent sulfate formation from London Fog to Chinese haze, *Proc. Natl. Acad. Sci. U.S.A.*,
 648 113, 13,630-13,635, 2016.

649 Wang, J., Liu, D., Ge, X., Wu, Y., Shen, F., Chen, M., Zhao, J., Xie, C., Wang, Q., Xu, W., Zhang, J.,
 650 Hu, J., Allan, J., Joshi, R., Fu, P., Coe, H., and Sun, Y.: Characterization of black carbon-containing
 651 fine particles in Beijing during wintertime, *Atmos. Chem. Phys.*, 19, 447-458,
 652 <https://doi.org/10.5194/acp-19-447-2019>, 2019.

653 Wang, Y., Zhang, F., Li, Z., Tan, H., Xu, H., Ren, J., Zhao, J., Du, W., and Sun, Y.: Enhanced
 654 hydrophobicity and volatility of submicron aerosols under severe emission control conditions in
 655 Beijing, *Atmos. Chem. Phys.*, 17, 5239-5251, <https://doi.org/10.5194/acp-17-5239-2017>, 2017.

656 Wang, Y., Li, Z., Zhang, Y., Du, W., Zhang, F., Tan, H., Xu, H., Fan, T., Jin, X., Fan, X., Dong, Z.,
 657 Wang, Q., and Sun, Y.: Characterization of aerosol hygroscopicity, mixing state, and CCN activity at
 658 a suburban site in the central North China Plain, *Atmos. Chem. Phys.*, 18, 11,739-11,752,
 659 <https://doi.org/10.5194/acp-18-11739-2018>, 2018.

660 Wang, Y., Li, Z., Zhang, R., Jin, X., Xu, W., Fan, X., Wu, H., Zhang, F., Sun, Y., Wang, Q., Cribb, M.,
 661 and Hu, D.: Distinct ultrafine- and accumulation-mode particle properties in clean and polluted urban
 662 environments, *Geophys. Res. Lett.*, 46, 10,918-10,925, <https://doi.org/10.1029/2019GL084047>, 2019.

663 Wang, Y., Wang, J., Li, Z., Jin, X., Sun, Y., Cribb, M., Ren, R., Lv, M., Wang, Q., Gao, Y., Hu, R.,
 664 Shang, Y., and Gong, W.: Contrasting aerosol growth potential in the northern and central-southern
 665 regions of the North China Plain: implications for combating regional pollution, *Atmos. Environ.*,
 666 267, 118723, <https://doi.org/10.1016/j.atmosenv.2021.118723>, 2021.

667 Wehner, B., Berghof, M., Cheng, Y. F., Achtert, P., Birmili, W., Nowak, A., Wiedensohler, A., Garland,
 668 R. M., Pöschl, U., and Hu, M.: Mixing state of nonvolatile aerosol particle fractions and comparison
 669 with light absorption in the polluted Beijing region, *J. Geophys. Res. Atmos.*, 114, 85-86, 2009.

670 Wu, Y., Wang, X., Tao, J., Huang, R., Tian, P., Cao, J., Zhang, L., Ho, K. F., Han, Z., and Zhang, R.:
 671 Size distribution and source of black carbon aerosol in urban Beijing during winter haze episodes,
 672 *Atmos. Chem. Phys.*, 17, 7965-7975, <https://doi.org/10.5194/acp-17-7965-2017>, 2017.

673 Wu, Z., Wang, Y., Tan, T., Zhu, Y., Li, M., Shang, D., Wang, H., Lu, K., Guo, S., Zeng, L., and Zhang,
 674 Y.: Aerosol liquid water driven by anthropogenic inorganic salts: implying its key role in haze
 675 formation over the North China Plain, *Environ. Sci. Tech. Lett.*, 5, 160-166,
 676 <https://doi.org/10.1021/acs.estlett.8b00021>, 2018.

677 Zhang, F., Wang, Y., Peng, J., Chen, L., Sun, Y., Duan, L., Ge, X., Li, Y., Zhao, J., Liu, C., Zhang, X.,
 678 Zhang, G., Pan, Y., Wang, Y., Zhang, A. L., Ji, Y., Wang, G., Hu, M., Molina, M. J., and Zhang, R.:
 679 An unexpected catalyst dominates formation and radiative forcing of regional haze, *Proc. Natl. Acad.*
 680 *Sci. U.S.A.*, 117, 3960, <https://doi.org/10.1073/pnas.1919343117>, 2020.

681 Yu, C., Liu, D., Broda, K., Joshi, R., Olfert, J., Sun, Y., Fu, P., Coe, H., and Allan, J. D.: Characterising
 682 mass-resolved mixing state of black carbon in Beijing using a morphology-independent measurement
 683 method, *Atmos. Chem. Phys.*, 20, 3645-3661, <https://doi.org/10.5194/acp-20-3645-2020>, 2020.

684 Zhang, S. L., Ma, N., Kecorius, S., Wang, P. C., Hu, M., Wang, Z. B., Größ, J., Wu, Z. J., and

带格式的: 字体: (默认) Times New Roman, (中文) + 中文正文 (等线), 10 磅, 英语(美国)

带格式的: 字体: (默认) Times New Roman, (中文) + 中文正文 (等线), 10 磅, 英语(美国)

带格式的: 字体: 10 磅, 字体颜色: 黑色

带格式的: 字体: (默认) Times New Roman, (中文) + 中文正文 (等线), 10 磅, 英语(美国)

带格式的: 字体: (默认) Times New Roman, (中文) + 中文正文 (等线), 10 磅, 英语(美国)

带格式的: 字体: 10 磅, 字体颜色: 黑色

685 Wiedensohler, A.: Mixing state of atmospheric particles over the North China Plain, Atmos. Environ.,
686 125, Part A, 152-164, <https://doi.org/10.1016/j.atmosenv.2015.10.053>, 2016.
687 Zhang, Y., Zhang, Q., Cheng, Y., Su, H., Kecorius, S., Wang, Z., Wu, Z., Hu, M., Zhu, T., Wiedensohler,
688 A., and He, K.: Measuring the morphology and density of internally mixed black carbon with SP2
689 and VTDMA: new insight into the absorption enhancement of black carbon in the atmosphere, Atmos.
690 Meas. Tech., 9, 1833-1843, <https://doi.org/10.5194/amt-9-1833-2016>, 2016.
691 Zhang, Y., Du, W., Wang, Y., Wang, Q., Wang, H., Zheng, H., Zhang, F., Shi, H., Bian, Y., Han, Y., Fu,
692 P., Canonaco, F., Prévôt, A. S. H., Zhu, T., Wang, P., Li, Z., and Sun, Y.: Aerosol chemistry and
693 particle growth events at an urban downwind site in North China Plain, Atmos. Chem. Phys., 18,
694 14,637-14,651, <https://doi.org/10.5194/acp-18-14637-2018>, 2018.
695 Zhang, Y., Liu, H., Lei, S., Xu, W., Tian, Y., Yao, W., Liu, X., Liao, Q., Li, J., Chen, C., Sun, Y., Fu, P.,
696 Xin, J., Cao, J., Pan, X., and Wang, Z.: Mixing state of refractory black carbon in fog and haze at
697 rural sites in winter on the North China Plain, Atmos. Chem. Phys., 21, 17631-17648,
698 <https://doi.org/10.5194/acp-21-17631-2021>,
699 Zhou, C., Zhang, H., Zhao, S., and Li, J.: Simulated effects of internal mixing of anthropogenic aerosols
700 on the aerosol-radiation interaction and global temperature, Int. J. Climatol., 37, 972-986, 2017.
701

带格式的: 字体: (默认) Times New Roman, (中文) + 中文正文 (等线), 10 磅, 英语(美国)

带格式的: 字体: (默认) Times New Roman, (中文) + 中文正文 (等线), 10 磅, 英语(美国)

带格式的: 字体: 10 磅, 字体颜色: 黑色